

Significant CO₂ photoreduction on a high-entropy oxynitride

Saeid Akrami¹, Parisa Edalati¹, Yu Shundo^{2,3}, Motonori Watanabe², Tatsumi Ishihara^{2,3,4}, Masayoshi Fuji^{1,5} and Kaveh Edalati^{2,3,*}

¹ Department of Life Science and Applied Chemistry, Nagoya Institute of Technology, Tajimi 507-0071, Japan

² WPI, International Institute for Carbon-Neutral Energy Research (WPI-I2CNER), Kyushu University, Fukuoka 819-0395, Japan

³ Mitsui Chemicals, Inc. - Carbon Neutral Research Center (MCI-CNRC), Kyushu University, Fukuoka 819-0395, Japan

⁴ Department of Applied Chemistry, Faculty of Engineering, Kyushu University, Fukuoka 819-0395, Japan

⁵ Advanced Ceramics Research Center, Nagoya Institute of Technology, Tajimi 507-0071, Japan

Abstract

CO₂ photoreduction on photocatalysts is a nature-friendly solution to decrease the CO₂ amount, but the method still has low efficiency because of difficult separation and easy recombination of charge carriers in available catalysts. In this study, a high-entropy oxynitride was introduced as an active photocatalyst for photoreduction. The material had a chemical composition of TiZrNbHfTaO₆N₃ and was produced by a high-pressure torsion method followed by oxidation and nitriding. It showed higher photocatalytic CO₂ to CO conversion compared to corresponding high-entropy oxide, benchmark photocatalyst P25 TiO₂, and almost all catalysts introduced in the literature. The high activity of this oxynitride, which also showed good chemical stability, was attributed to the large absorbance of light and easy separation of electrons and holes, the low recombination of charge carriers, and the high CO₂ adsorption on the surface. These findings introduce high-entropy oxynitrides as promising photocatalysts for CO₂ photoreduction.

Keywords: High-entropy alloy; high-entropy ceramics; photocatalysis; bandgap narrowing; CO₂ photoreduction

*Corresponding author:

Kaveh Edalati (E-mail: kaveh.edalati@kyudai.jp; Tel: +81-92-802-6744)

1.Introduction

Global warming by significant CO₂ emission is a universal concern in recent years which has forced scientists and politicians to find a remedy to convert this harmful gas into useful substances [1,2]. CO₂ photoreduction as an artificial photosynthesis method is a clean strategy that can transform CO₂ into reactive or valuable components like CO and CH₄ [1,2]. CO₂ photoreduction takes place on the surface of a photocatalyst (usually a semiconductor) under irradiation by solar light. Electrons in the valence band of the photocatalyst absorb the light and transfer into the conduction band and misplace the holes within the valence band [1,2]. Exited holes and electrons take part in reactions for oxidation and reduction, respectively, and produce CO, CH₄ and other hydrocarbons [1,2]. The challenge in this field is to discover an appropriate photocatalyst with high light absorbance, low bandgap, appropriate band positions, a low recombination rate of electrons and holes, high CO₂ adsorbance and high chemical stability [3,4].

Oxide photocatalysts such as TiO₂ [5,6] are the most common photocatalysts with high stability for CO₂ photoreduction application, but they have large bandgaps such as 3.1 eV for TiO₂ [5,6]. In contrast, there are some reports on photocatalytic activity of nitrides such as TaN [7] and C₃N₄ [8] for CO₂ conversion which have lower bandgaps compared to oxides, but nitrides are not chemically so stable [7,8]. To solve the problem of oxide and nitride photocatalysts in terms of large bandgap and low stability, respectively, oxynitrides were recommended as low bandgap and highly stable catalysts for photocatalysis [9]. Oxynitrides have been widely used for photocatalytic water splitting; however, only limited oxynitrides such as α -Fe₂O₃/LaTiO₂N [10] and TaON [11,12] were used for photocatalytic CO₂ conversion. Significant electron-hole recombination, sluggish kinetics, the low tendency for CO₂ adsorption and relatively low stability in the co-presence of CO₂ and water are some reasons for limited application of metal oxynitrides for photocatalytic CO₂ conversion [10,13]. Therefore, introducing a strategy to solve all or some of these problems is a key issue in using the benefits of oxynitrides for CO₂ conversion. Simultaneous addition of several principal elements and production of high-entropy oxynitride ceramics can be an effective strategy, although there have been few attempts in this regard.

High-entropy ceramics containing at least five cations and having a configurational entropy of larger than $1.5R$, where R is the molar gas constant, are new remarkable candidates for various applications due to their superior stability, large lattice defects/strain and heterogenous valence electron distribution [14,15]. Among various kinds of high-entropy ceramics, high-entropy oxides (HEOs) have become quite popular due to their feasibility for various applications. Catalysis is a new application field for highly stable HEOs which has been expanded in recent years as a top issue [16]. These oxides have been used as electrocatalyst for oxygen evolution [17-19], catalyst for CO oxidation [20-22], catalyst in lithium-sulfur batteries [23], electrocatalyst for CO₂ conversion [24], electrocatalyst in electrochemical capacitors [25], catalyst for combustion reactions [26], and photocatalyst for redox reactions [27,28]. High entropy nitrides (HENs) are another popular type of high-entropy ceramics and have been used as coatings [29], supercapacitors [30] and solar selective absorbers [31]. A combination of the perception of metal oxynitrides as low bandgap photocatalysts and high-entropy ceramics as highly stable materials can be a new strategy to expand the application of oxynitrides for photocatalytic CO₂ conversion. Although high-entropy oxynitrides (HEONs) were successfully synthesized in a few studies [32,33], there are no reports on the photocatalytic performance of HEONs for CO₂ photoreduction.

In this study, a two-phase TiZrNbHfTaO₆N₃ was synthesized as the first HEON for photocatalytic CO₂ conversion by high-pressure torsion mechanical alloying [34] and subsequent oxidation and nitriding. The HEON showed better light absorbance, lower charge carrier

recombination rate, higher CO₂ adsorbance and larger photocatalytic CO₂ conversion compared to relevant HEO (TiZrNbHfTaO₁₁) and benchmark photocatalyst P25 TiO₂. Moreover, the activity of the HEON was higher than almost all photocatalysts developed in the literature for CO₂ photoreduction. These findings open a path to develop new high-entropy photocatalysts with significant efficiency for CO₂ photoreduction.

2. Experimental procedures

Despite various synthesis methods reported in the literature to produce HEOs [14-28] and HENs [14,15,29-31], the HEON was fabricated using a three-step synthesis method for this study [33]: (i) severe plastic deformation through the high-pressure torsion (HPT) method for alloying pure elemental powders [34,35], (ii) oxidation at elevated temperature and (iii) nitriding at elevated temperature. First, titanium (99.9%), zirconium (95.0%), niobium (99.9%), hafnium (99.5%) and tantalum (99.9%) powders with the same molar fraction of 0.2 were dispersed in acetone, mixed using ultrasonic and dried in air. About 700 mg of powder mixture was compacted into a 10 mm diameter disc under a pressure of 0.4 GPa and further proceeded by HPT under 6 GPa at room temperature using a rotation rate of one turn per minute for 100 turns to achieve a single-phase (body-centered cubic, BCC) alloy. Second, the HPT-processed high-entropy alloy was crushed in a mortar and inserted into a furnace for 24 h under a hot (1373 K) air atmosphere to generate the HEO, TiZrNbHfTaO₁₁ with dual monoclinic (40 wt%) and orthorhombic (60 wt%) structures. Third, the HEO was processed by nitriding in ammonia at 1373 K for 7 h using a heating rate of 20 Kmin⁻¹ with an NH₃ flow of 150 mLmin⁻¹ to generate a two-phase (40 wt% monoclinic + 60 wt% face-centered cubic, FCC) HEON, TiZrNbHfTaO₆N₃. The fabricated HEON was characterized by different methods, as follows.

The crystallographic features were analyzed by X-ray diffraction (XRD) using a Cu K α source having 0.1542 nm wavelength. Phase fractions and lattice parameters were measured by the Rietveld analysis in the PDXL software.

The composition was examined by dispersing the sample on a carbon tape and conducting energy-dispersive X-ray spectroscopy (EDS) in a scanning electron microscope (SEM) under 15 keV.

The microstructure was examined by dispersing the crushed sample on carbon grids and employing a transmission electron microscope (TEM) under 200 keV by taking high-resolution (HR) images and analyzing them by fast-Fourier transform (FFT). Moreover, the distribution of elements was examined by a scanning-transmission electron microscope (STEM) under 200 kV by taking high-angle annular dark-field (HAADF) micrographs and conducting EDS analysis.

X-ray photoelectron spectroscopy (XPS) was performed to determine the top of the valence band and the electronic state of each element using a Mg K α source.

The absorbance of light, and band structure including the level of bandgap were evaluated by UV-vis diffuse reflectance spectroscopy (followed by Kubelka-Munk calculation) and X-ray/UV photoelectron spectroscopy (XPS and UPS). The valence band top was determined by the UPS and XPS analyses and the conduction band bottom was determined by subtracting the bandgap value from the valence band top.

The electron-hole recombination was evaluated by photoluminescence (PL) spectroscopy using a UV laser (325 nm wavelength).

Photocurrent measurement on thin films of the samples was performed using the full arc of a Xe lamp in a 1 M Na₂SO₄ electrolyte. The experiments were conducted in the potentiostatic

amperometry mode during the time (180 s light ON and 180 s light OFF) using an electrochemical analyzer. The counter and reference electrodes were Pt wire and Ag/AgCl, respectively, and the external potential was 0.7 V vs. Ag/AgCl. To prepare the thin films, 5 mg of each sample was crushed in 0.2 mL ethanol, spread on the FTO glass (fluorine-doped tin oxide with 2.25 mm thickness and $15 \times 25 \text{ mm}^2$ surface area), and annealed at 473K for 2 h.

Diffuse reflectance infrared Fourier transform (DRIFT) spectrometry was performed to understand the adsorbance mode of CO₂ on the surface of each photocatalyst. First, 50 mg of each sample was treated at 773 K for 1 h in an argon atmosphere. Then, argon was replaced by 100% CO₂ gas at 773 K and the samples were kept under this condition for 30 min. The samples were then cooled down to room temperature and the CO₂ gas was replaced with argon. After keeping the samples in argon for 30 min, the DRIFT spectroscopy was conducted.

CO₂ photoreduction was examined in a cylindrical-shaped quartz photoreactor with 858 mL inner volume and specifications described in detail earlier [28]. Light source was placed in a space inside the photoreactor and CO₂ flow entered the reactor from a gas cylinder by a hole on the top of the reactor. Outlet gas from the reactor partly entered a gas chromatograph for the gas analysis and mainly flew to a vent. For the photoreduction experiments, 100 mg of HEON photocatalyst were dispersed in a 500 mL solution of 1 M NaHCO₃ and pure water. CO₂ gas was injected into the mixture (3 mLmin⁻¹) and the mixture was continuously stirred by a magnetic stirrer. It should be noted that the temperature was kept constant at 288 K utilizing a water chiller. To be sure about the nonappearance of reaction products without irradiating the mixture, the experiments were first performed for 2 h in dark conditions. Then the photocatalytic experiment was performed under irradiation of a 400 W high-pressure mercury lamp (HL400BH-8 of Sen Lights Corporation) with 0.5 Wcm⁻² light intensity without any filtration. The gas of the photoreactor was analyzed using gas chromatography (GC-8A of Shimadzu). The generation of CH₄ and CO was analyzed using a methanizer and flame-ionization detector. The generation of oxygen and hydrogen was analyzed using a thermal conductivity detector. A blank test was conducted without catalyst addition under light irradiation and CO₂ injection to confirm that no CO was produced from other sources in the experimental system. Another blank test was conducted with catalyst addition under light irradiation and argon injection to confirm that CO was not produced without CO₂ injection.

3. Results

Fig. 1a illustrates the XRD profile of HEON. The HEON has two cubic (Fm3m space group, $a=b=c=0.459 \text{ nm}$; $\alpha=\beta=\gamma=90^\circ$) and monoclinic (P21/c space group, $a=0.512$, $b=0.517$, $c=0.530 \text{ nm}$; $\alpha=\gamma=90^\circ$, $\beta=99.2^\circ$) phases with 60 and 40 wt% fractions, respectively. **Fig. 1b** illustrates the EDS profile of the HEON. The EDS analysis suggests a general composition of TiZrHfNbTaO₆N₃ for the synthesized HEON. The presence of two phases should be due to the thermodynamics of the Ti-Zr-Hf-Nb-Ta-O-N system at the synthesis temperature. The existence of two phases can be beneficial for charge separation in photocatalysis because the phase boundaries can act as heterojunctions for charge carrier migrations [36,37]. Although first-principle electronic structure calculations are required to clarify the migration direction of charge carriers in this HEON, it is expected that photoexcited electrons in the conduction band of one phase with a higher energy level move to the conduction band of the other phase and exited holes transfer from the valence band of one phase with the lower energy level to the valence band of another phase [36,37].

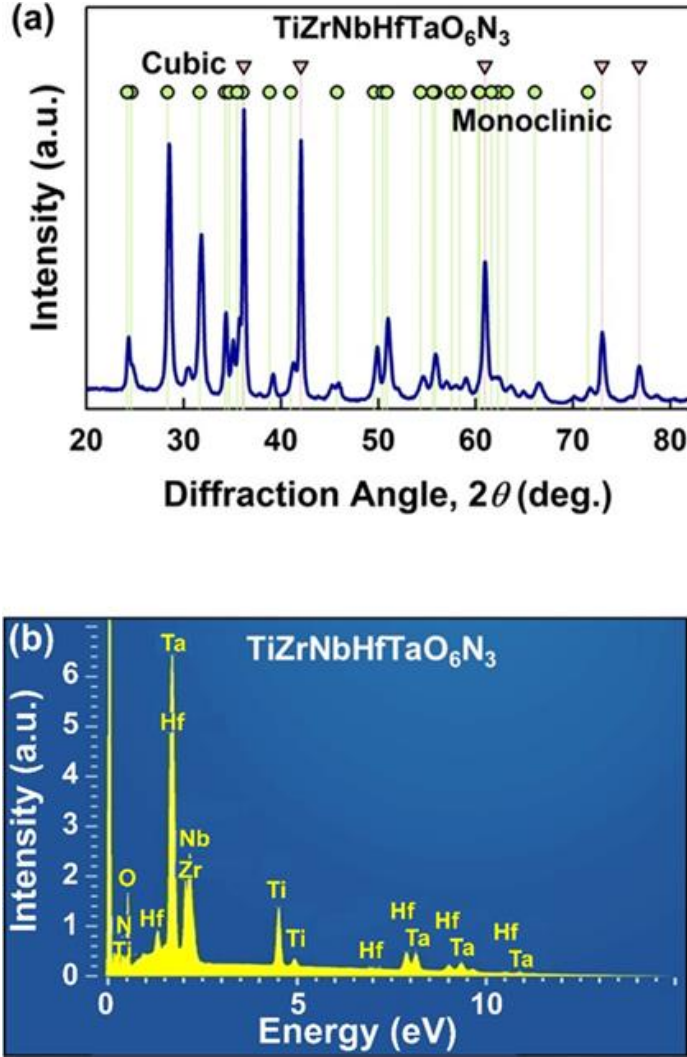


Fig. 1. Formation of high-entropy oxynitride with cubic and monoclinic phases and chemical composition of $\text{TiZrNbHfTaO}_6\text{N}_3$. a) XRD profile and b) EDS spectrum of high-entropy oxynitride.

The microstructure of the HEON is shown in **Fig. 2** using different methods. **Fig. 2a** illustrates a micrograph taken by SEM, which indicates that the HEON contains large powders with an average size of 20 μm . **Fig. 2b** shows a HR image taken by TEM confirming the existence of nanocrystals of cubic and monoclinic phases which agrees with the XRD analysis. It also indicates the existence of a large fraction of interphases that can act as heterojunctions [1]. **Fig. 2c** illustrates a HAADF micrograph with relevant EDS mappings taken by STEM, showing a reasonably homogenous distribution of elements at the nanometer scale. Slight differences in the distribution of metallic elements, oxygen and nitrogen should be mainly due to the presence of two phases. Here, it should be noted that XPS analyses, shown in **Supporting Information Fig. S1**, confirm that the main states of elements are Ti^{4+} , Zr^{4+} , Hf^{4+} , Nb^{5+} , Ta^{5+} , O^{2-} and N^{3-} .

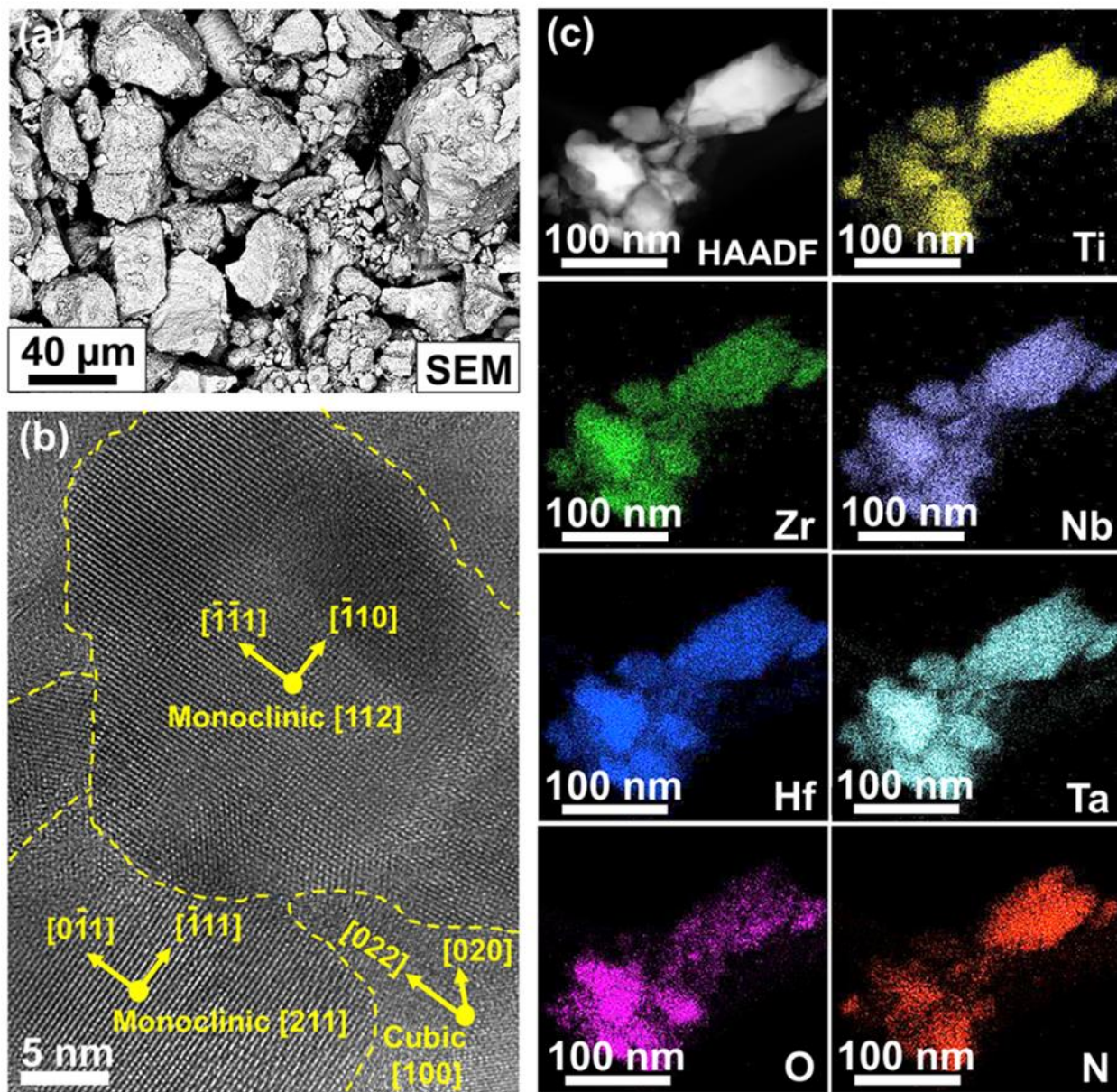


Fig. 2. Formation of nanocrystalline monoclinic and cubic phases with uniform elemental distribution in high-entropy oxynitride powder. a) SEM micrograph, b) HR micrograph and c) STEM-HAADF micrograph and relevant EDS mappings for high-entropy oxynitride.

Fig. 3a shows the light absorbance of the HEON in comparison with the relevant HEO as well as the P25 TiO₂ photocatalyst. The HEON exhibits significant light absorbance compared with the HEO and P25 TiO₂. According to the Kubelka-Munk calculation, the bandgap for the HEON is 1.6 eV which is extremely narrower compared with the bandgap of the HEO (3.0 eV) and P25 (3.1 eV) [28]. **Fig. 3b** shows the electronic band structure of the three mentioned materials including the appearance of three samples. A color change from white and orange for P25 TiO₂ and the HEO occurs to dark brown for the HEON, confirming the high light absorbance of the HEON in good

agreement with the UV-vis absorbance data [38]. The electronic band structures were determined by considering the bandgaps calculated using the Kubelka-Munk theory, the top of the valence band was measured by XPS spectroscopy, and the bottom of the conduction band was calculated by subtracting the bandgap from the top of the conduction band. The bandgap for the P25 TiO₂, the HEO and the HEON are 3.0, 3.0 and 1.6 eV, respectively; the values for the top of the valence band are 2.2, 1.8 and 1.3 eV vs. NHE for P25 TiO₂, the HEO and the HEON, respectively; and the values for the bottom of the conduction band are -0.8, -1.2 and -0.3 eV vs. NHE for P25 TiO₂, the HEO and the HEON, respectively. As shown in Fig. 3b, the band structure of the HEON indicates its low bandgap with appropriate positions of the valence band top and the conduction band bottom for various CO₂ conversion reactions [39]. The low bandgap of this HEON can lead to easy separation of electrons and holes during photocatalysis.

Fig. 3c shows the photoluminescence spectra of the three materials to examine the electron-hole recombination. P25 TiO₂ and the HEO have almost the same photoluminescence intensity while the HEON shows the lowest photoluminescence. The absence of an intensive photoluminescence peak for the HEON confirms the significant suppression of electron-hole recombination which is a principal requirement for the enhancement of photocatalytic reactions [2,3]. These results show that the main problem of metal oxynitrides in terms of high electron-hole recombination [11,13] can be solved by the strategy used in this study through the concept of high-entropy ceramics.

Fig. 3d shows the photocurrent measurement for the three samples. Due to the different particle sizes of these three samples and their dissimilarities in making binding to the FTO glass, their current density cannot be compared quantitatively; however, the shape of their photocurrent curves can clarify their different behaviors. For P25 TiO₂ there is a spike peak at the beginning of irradiation, but the current density decreases rapidly to a steady state, suggesting that electron-hole separation is followed by fast recombination. For the HEO the photocurrent curve under irradiation is almost a straight horizontal line which shows a better electron-hole separation of the HEO compared to P25 TiO₂. For the HEON, the current density increases by irradiation and reaches a steady state, suggesting that the ratio of electron-hole recombination to separation is the lowest for the HEON. After stopping the irradiation, the HEON still shows some reduced photocurrent due to the remained excited charge carriers, while P25 TiO₂ exhibits almost no photocurrent under the dark condition. The successful photocurrent generation on this HEON with an appropriate ratio of electron-hole separation to recombination suggests the potential of this material to act as a catalyst for CO₂ photoreduction [28,38].

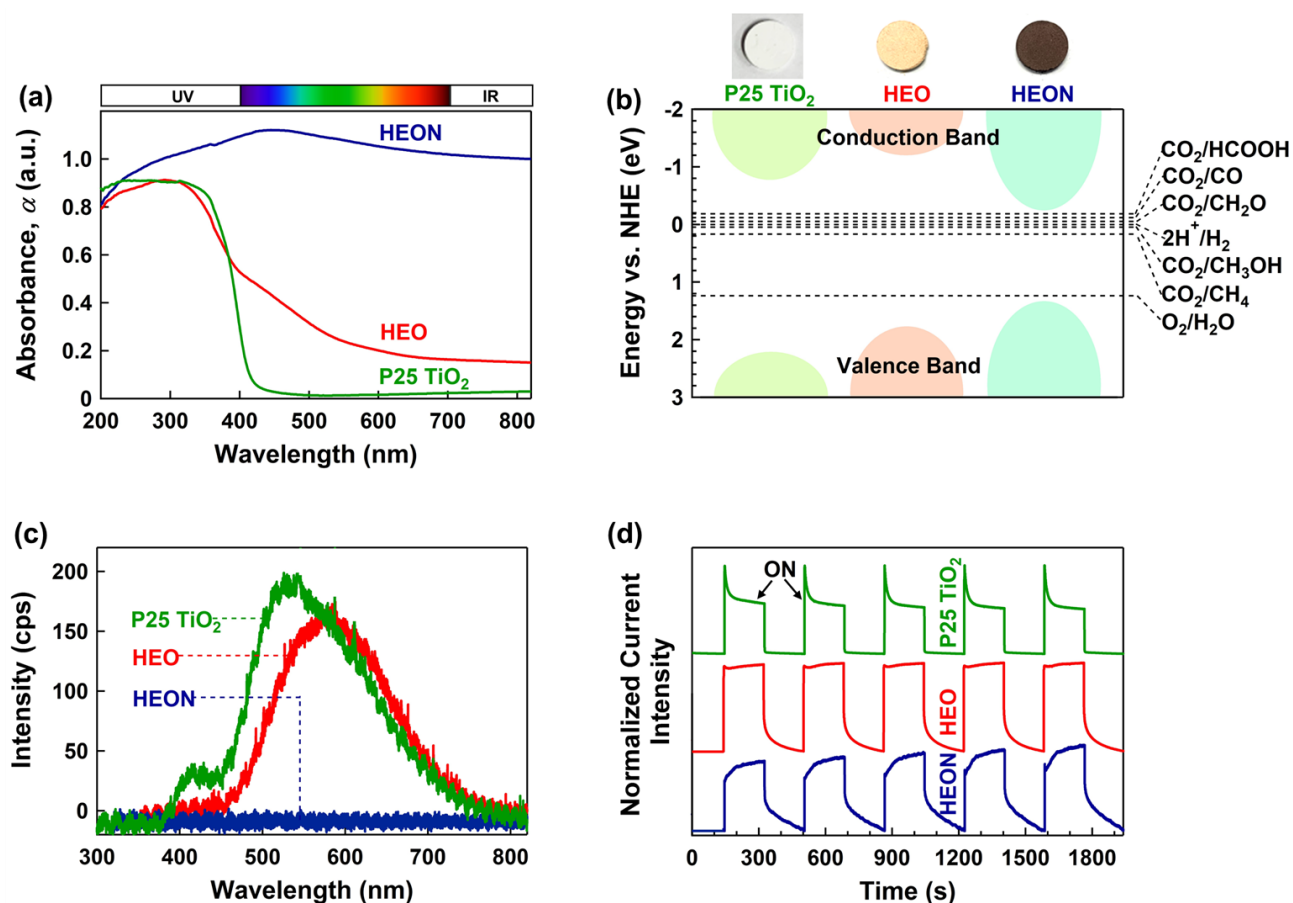


Fig. 3. High light absorbance, appropriate electronic band structure and low electron-hole recombination in high-entropy oxynitride. a) UV-vis spectra, b) electronic band structures including chemical potential for CO₂ conversion reactions and sample color, c) steady-state photoluminescence spectra and d) photocurrent generation of high-entropy oxynitride (HEON) in comparison with corresponding high-entropy oxide (HEO) and P25 TiO₂.

Fig. 4a compares the CO production rate of the HEON with the relevant HEO and P25 TiO₂ benchmark photocatalyst. Photoreduction of CO₂ to CO on the HEON is considerably better than the HEO and P25. The CO production rate for the HEON reaches 14.3 $\mu\text{molh}^{-1}\text{g}^{-1}$ after 1 h; and then decreases to a constant level after 3 h. The deviations in the reaction rate in the first two hours should be due to the time needed to reach an equilibrium condition in the measurement system. The average CO production rate for this HEON is $11.6 \pm 1.5 \mu\text{molh}^{-1}\text{g}^{-1}$ after 5 h, while the HEO and P25 have lower photocatalytic CO production rates of $4.6 \pm 0.3 \mu\text{molh}^{-1}\text{g}^{-1}$. **Fig. 4b** shows the photocatalytic activity of the HEON for H₂ production and compares it with the HEO and P25 TiO₂. This figure indicates that the efficiency of the HEON is much better than the HEO and P25 for photocatalytic H₂ production. The average H₂ production rate for the HEON is $5.1 \pm 0.5 \mu\text{molh}^{-1}\text{g}^{-1}$, while the rate for the HEO and P25 TiO₂ is 1.3 ± 0.1 and $1.5 \pm 0.1 \mu\text{molh}^{-1}\text{g}^{-1}$, respectively. To confirm the high activity and stability of this HEON for CO₂ photoreduction, a long-term photocatalytic experiment for 20 h was conducted on the sample after storage in air for 7 months. As shown with dashed-line curves in **Fig. 4a** and **4b**, the material still shows high activity with a

constant CO and H₂ production rate, although the reaction rates are slightly lower than in the first experiment.

Here, three issues regarding the photocatalytic tests should be mentioned. First, no CO was detected in three blank tests: (i) with catalyst addition and CO₂ injection under dark conditions, (ii) without catalyst addition under light irradiation and CO₂ injection, and (iii) with catalyst addition under light irradiation and argon injection. Second, despite the high light absorbance of HEON in the visible light and near-infrared region, the material did not show any photocatalytic activity in these regions within the detection limits of gas chromatographs. Third, despite the higher feasibility of CH₄ production compared to CO generation in terms of thermodynamics, no CH₄ was detected for these materials which can be explained by the kinetics of reactions. Due to the requirement of CH₄ production to more electrons and protons, its production is not kinetically more feasible than CO production [40,41]. On the other hand, once CO is produced, it does not tend to be adsorbed on active sites and thus the reaction terminates with the CO production [42].

Fig. 4c illustrates the XRD profiles of HEON before and after photocatalysis. The profiles indicate that the crystal structures do not change after photoreduction, suggesting that the HEON remains stable after photocatalytic CO₂ conversion. The high stability of TiZrHfNbTaO₆N₃ is partly because of the entropy-stabilization concept which leads to low Gibbs free energy in the presence of a large number of elements [14,15]. This high stability is an important issue that has led to the utilization of high-entropy ceramics for various applications with superior performance [14-33].

Fig. 4d shows the DRIFT spectra for the three samples to investigate the adsorbance mode of CO₂ on the surface of each photocatalyst. There is a peak at 665 cm⁻¹ which corresponds to CO₃²⁻ [43] and another one at 2340-2360 cm⁻¹ which is relevant to CO₂ gas in the beamline of spectrometer or to physically adsorbed CO₂ on photocatalysts [44]. The intensity of both peaks is the maximum for the HEON, but it is hard to discuss about physically adsorbed CO₂ using the peak at 2340-2360 cm⁻¹ due to the possible differences in the CO₂ gas concentration in the beamline. The peak at 665 cm⁻¹ for P25 TiO₂ is so weak, but its intensity is the highest for the HEON, suggesting CO₂ can bond to the surface as carbonate. Since CO₂ is a Lewis acid, the basic active sites have a significant role in the adsorption and activation of this molecule [45]. P25 TiO₂ is considered a weak acid and chemisorption of CO₂ in the form of carbonate is weak on the surface of this material. The high intensity of carbonate peak on the HEON suggests that the concentration of basic active sites is higher in this material. These DRIFT experiments indicate the higher capability of the HEON for physisorption and chemisorption of CO₂ compared to the HEO and P25 TiO₂.

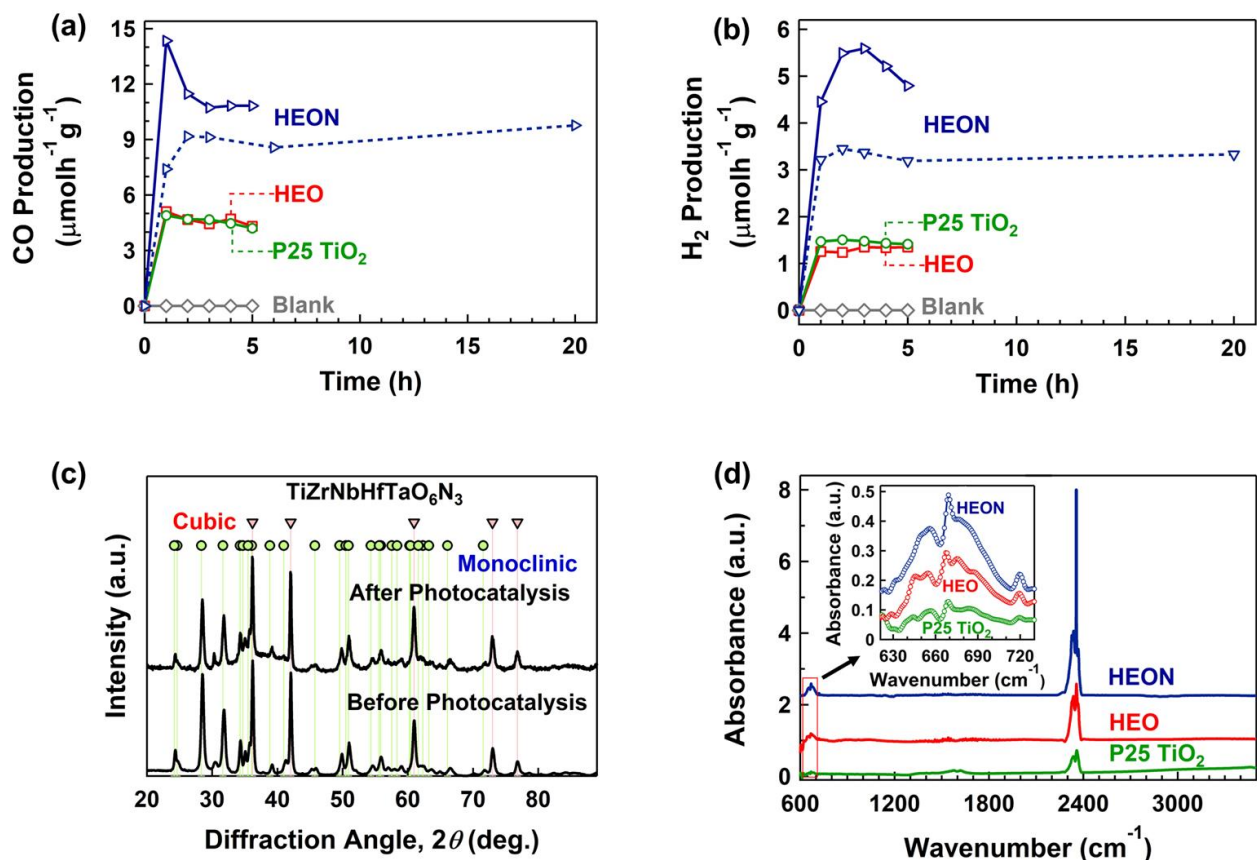


Fig. 4. High efficiency of high-entropy oxynitride for photocatalytic CO and hydrogen production. Rate of (a) CO_2 to CO photoreduction and (b) hydrogen generation versus UV irradiation time for high-entropy oxynitride (HEON) compared to corresponding high-entropy oxide (HEO) and P25 TiO_2 . (c) XRD profiles before and after photocatalysis for high-entropy oxynitride. (d) DRIFT spectra of three samples.

4. Discussion

Three points need to be discussed in detail here: (i) the mechanism of photocatalytic CO production, (ii) the reasons for the high activity of the HEON, and (iii) the comparison of the activity of current HEON with other photocatalysts reported so far in the literature.

Regarding the first issue, it should be noted that the first step in photocatalytic CO_2 reduction process is the formation of $\text{CO}_2^{\bullet-}$ intermediate which is produced by sharing the electrons between CO_2 and photocatalyst surface [46]. Chemisorption of CO_2 molecules on photocatalyst surface to produce $\text{CO}_2^{\bullet-}$ occurs in three modes. (1) Nucleophilic bonding between oxygen atoms and catalyst surface (oxygen coordination), (2) electrophilic bonding between carbon atoms and catalyst surface (carbon coordination) and (3) mixed coordination between both oxygen and carbon atoms in CO_2 molecules with catalyst surface [46]. The chemistry of photocatalyst influences the bonding of $\text{CO}_2^{\bullet-}$ with catalyst surface and determine the reaction pathway [46]. If a photocatalyst contains Sn, Pb, Hg, In, and Cd metals, then it has a tendency to oxygen coordination to produce OCHO^{\bullet} as an intermediate and formic acid (HCOOH) as the final product. Photocatalysts containing noble and transition metals have a tendency to carbon coordination which leads to producing CO^{\bullet} and OCHO^{\bullet} as intermediates. Since the bonding between CO^{\bullet} and

catalyst surface is weak, CO is usually the main product in this coordination. If a photocatalyst consists of Cu atoms, then $\cdot\text{CO}$ and $\cdot\text{OCHO}$ are produced as intermediates, but because of the strong bonding between $\cdot\text{CO}$ and Cu, other hydrocarbons such as methane (CH_4) and ethanol ($\text{C}_2\text{H}_5\text{OH}$) are usually formed as final products [46]. In this study, since the HEON, the HEO and P25 TiO_2 consist of transition metals, the carbon coordination pathway occurs for these photocatalysts which leads to CO production. This pathway has the following reactions [46].



Regarding the second issue, it should be considered that combining the concepts of metal oxynitrides and high-entropy ceramics was the spark starter of this study. Metal oxynitrides have been introduced as promising low-bandgap photocatalysts particularly for water splitting [9], while their application for CO_2 conversion is still in the initial steps [10-12]. The reason for the low bandgap of oxynitrides compared to oxide photocatalysts is that the valence band top of these materials is generated using hybridized 2p oxygen and nitrogen orbitals, but it is generated using only 2p oxygen orbitals in oxides. Since the energy level for nitrogen 2p orbitals is higher than oxygen 2p orbitals, the bandgap of oxynitrides is smaller than oxides [9]. However, these metal oxynitrides suffer from significant recombination of charge carriers and modest stability [10,13].

High-entropy ceramics are promising new materials with interesting properties because of the presence of multiple elements which leads to superior stability, large lattice defects/strain and heterogenous valence electron distribution [14,15]. The presence of various elements in the lattice of high-entropy ceramics leads not only to high configurational entropy and resultant high chemical stability for catalysis but also to lattice distortion and formation of inherent point defects such as vacancies which can act as active sites for catalysis [47]. Although future theoretical studies are required to determine the active sites in high-entropy photocatalysts, it was shown in conventional photocatalysts that vacancies on the surface adsorb CO_2 and activate it by decreasing the bonding energy between carbon and oxygen [42,46]. These vacancies trap electrons and act as active sites and lead to the improved photocatalytic activity for CO_2 reduction, but their fraction should be optimized to achieve the highest activity and best reaction selectivity [48,49].

The combination of the two concepts of oxynitrides and high-entropy ceramics led to the introduction of $\text{TiZrNbHfTaO}_6\text{N}_3$ as a highly stable and low-bandgap photocatalyst for CO_2 conversion with much better photocatalytic performance compared with P25 TiO_2 . Such a high activity is particularly interesting because the surface area of the HEON is much smaller than P25 TiO_2 : $2.3 \text{ m}^2\text{g}^{-1}$ for the HEON and $38.7 \text{ m}^2\text{g}^{-1}$ for P25 TiO_2 measured by the Brunauer-Emmett-Teller (BET) technique in the nitrogen atmosphere. The high activity of the HEON for CO_2 photoreduction can be attributed to high light absorbance (i.e., easy electron-hole separation), appropriate band positions compared to chemical potentials for reactions, and low electron-hole recombination, and high surface CO_2 adsorption [1,2]. The presence of interphase boundaries in this HEON can also partly contribute to the easy separation of charge carriers and improvement of photocatalytic activity [1].

Regarding the third issue, although the comparison between the current HEON and P25 TiO_2 using similar experimental procedures confirms the high photocatalytic activity of the HEON, it is worth comparing the activity of this HEON with the given data in the literature. Photocatalysis in various studies is performed in different conditions in terms of photoreactor type, temperature, catalyst concentration, CO_2 flow rate, type of light source and concentration of reactants, and thus,

a comparison between different studies should be evaluated with care. The CO production rate per catalyst mass and catalyst surface area are given in **Table 1** in comparison with reported photocatalysts in the literature [49-80]. Since photocatalysis occurs on the surface, normalizing the CO production rate per surface area should be more reasonable for comparison purposes. According to **Table 1**, the rate of CO production in the literature fluctuates in the 0.00095-1.33 $\mu\text{molh}^{-1}\text{m}^{-1}$ range, while the CO generation rate of $4.66 \pm 0.3 \mu\text{molh}^{-1}\text{m}^{-1}$ on the HEON is higher than all these reported data. Moreover, the HEON shows much better activity per both surface area and mass unit compared to other oxynitrides reported in the literature. Although these findings introduce HEON as the most effective photocatalyst for CO₂ photoreduction, future studies should focus on decreasing the particle size of these materials to increase their specific surface area.

Table 1. Photocatalytic CO₂ to CO conversion rate on high-entropy oxynitride compared to reported photocatalysts. For some catalysts which surface area was not reported in literature, CO production rate in $\mu\text{molh}^{-1}\text{m}^{-1}$ was not given.

Photocatalyst	Catalyst Concentration	Light Source	CO Production Rate ($\mu\text{molh}^{-1}\text{g}^{-1}$)	CO Production Rate ($\mu\text{molh}^{-1}\text{m}^{-1}$)	Ref.
TiO ₂ / Carbon Nitride Nanosheet	25 mg (Gas System)	150 W Xenon	2.04	----	[50]
TiO ₂ / Graphitic Carbon	100 mg (Gas System)	300 W Xenon	10.16	0.04	[51]
TiO ₂ Nanosheets Exposed {001} Facet	1 gL ⁻¹ (Liquid system)	Two 18 W Low-Pressure Mercury	0.12	0.00095	[52]
TiO ₂ / CoOx Hydrogenated	50 mg (Gas System)	150 W UV	1.24	0.0045	[53]
TiO ₂ 3D Ordered Microporous / Pd	100 mg (gas system)	300 W Xenon	3.9	0.066	[54]
Pt ²⁺ -Pt ⁰ / TiO ₂	100 mg (Gas System)	300 W Xenon	~12.14	0.7	[55]
Anatase TiO ₂ Hierarchical Microspheres	200 mg (Gas System)	40 W Mercury UV	18.5	0.37	[56]
TiO ₂ and Zn(II) Porphyrin Mixed Phases	60 mg (Gas System)	300 W Xenon	8	0.062	[57]
Anatase TiO ₂ Hollow Sphere	100 mg (Gas System)	40 W Mercury UV	14	0.16	[58]
Anatase TiO ₂ Nanofibers	50 gL ⁻¹ (Liquid System)	500 W Mercury Flash	40	----	[59]
C ₃ N ₄ by Thermal Condensation	100 mg (Gas System)	350 W Mercury	4.83	-----	[60]
Cd _{1-x} Zn _x S	45 mg (Gas System)	UV-LED irradiation	2.9	0.015	[61]
BiOI	150 mg (Gas System)	300 W High-Pressure xenon	4.1	0.03	[62]
xCu ₂ O / Zn _{2-2x} Cr	4 gL ⁻¹ (Liquid System)	200 W Mercury-Xenon	2.5	0.018	[63]
CeO _{2-x}	50 mg (Gas System)	300 W Xenon	1.65	0.08	[64]
Cu ₂ O / RuO _x	500 mg (Gas System)	150 W Xenon	0.88	---	[65]
Bi ₂ Sn ₂ O ₇	0.4 gL ⁻¹ (Liquid System)	300 W xenon	14.88	0.24	[66]
Ag / Bi / BiVO ₄	10 mg (Gas System)	300W Xenon Illuminator	5.19	0.42	[67]
g-C ₃ N ₄ / BiOCl	20 mg (Gas System)	300 W High-Pressure Xenon	4.73	---	[68]
Fe / g-C ₃ N ₄	1 gL ⁻¹ (Liquid System)	300 W Xenon	~22.5	0.06	[69]
Bi ₂ MoO ₆	0.7 gL ⁻¹ (Liquid System)	300 W Xenon	41.5	1.26	[70]
Bi ₂₄ O ₃₁ C ₁₀	50 mg (Gas System)	300 W High-Pressure Xenon	0.9	---	[71]
g-C ₃ N ₄ / Zinc Carbodiimide / Zeolitic Imidazolate Framework	100 mg (Gas System)	300 W Xenon	~0.45	0.014	[72]
BiVO ₄ / C / Cu ₂ O	---	300 W Xenon	3.01	----	[73]
g-C ₃ N ₄ / α -Fe ₂ O ₃	200 mg (Gas System)	300 W Xenon	5.7	----	[74]
Bicrystalline Anatase/Brookite TiO ₂ Microspheres	30 mg (Gas System)	150 W Solar Simulator	145	0.95	[75]
10 wt % In-Doped Anatase TiO ₂	250 mg (Gas System)	500 W Mercury Flash	81	1.33	[76]
10 wt % Montmorillonite-Loaded TiO ₂	50 mg (Gas System)	500 W Mercury	103	1.25	[77]
Bi ₄ O ₅ Br ₂	20 mg (Gas System)	300 W High-Pressure Xenon	63.13	0.58	[78]
ZnGaON	---	1600 W Xenon	1.05	---	[79]
WO ₃ / LaTiO ₂ N	10 mg (Gas System)	300 W Xenon	2.21	0.4	[80]
α -Fe ₂ O ₃ / LaTiO ₂ N	20 mg (Gas System)	300 W Xenon	9.7	0.65	[10]
RuRu / Ag / TaON	1 gL ⁻¹ (Liquid System)	High-Pressure Mercury	5	----	[11]
RuRu / TaON	1 gL ⁻¹ (Liquid system)	High-Pressure Mercury	3.33	----	[11]
Ag / TaON / RuBLRu'	2 gL ⁻¹ (Liquid System)	500 W High-Pressure Mercury	0.056	----	[12]
TiZrHfNbTaO ₆ N ₃	0.2 gL ⁻¹ (Liquid System)	400 W High-Pressure Mercury	10.7 ± 1.8	4.7 ± 0.3	This study

4. Conclusion

This study introduced a high-entropy oxynitride with low bandgap, low electron-hole recombination, high CO₂ adsorbance and high chemical stability for photocatalytic CO₂ conversion. The material, which was synthesized using high-pressure torsion and subsequent oxidation and nitriding, had two phases of face-centered cubic and monoclinic with a chemical composition of TiZrNbHfTaO₆N₃. The material had better photocatalytic CO₂ conversion performance compared with corresponding high-entropy oxide, benchmark photocatalyst P25 TiO₂ and all reported photocatalysts in the literature. These findings open a new path to developing highly efficient photocatalysts for CO₂ conversion.

Acknowledgments

This study is supported partly by the Mitsui Chemicals, Inc., Japan, partly by Hosokawa Powder Technology Foundation, Japan, and partly through Grants-in-Aid from the Japan Society for the Promotion of Science (JSPS), Japan (JP19H05176 & JP21H00150).

References

- [1] K. Li, B. Peng, T. Peng, Recent advances in heterogeneous photocatalytic CO₂ conversion to solar fuels, *ACS Catal.* 6 (2016) 7485-7527.
- [2] J. Ran, M. Jaroniec, S.Z. Qiao, Cocatalysts in semiconductor-based photocatalytic CO₂ reduction: achievements, challenges, and opportunities, *Adv. Mater.* 30 (2018) 1704649.
- [3] W. Tu, Y. Zhou, Z. Zou, Photocatalytic conversion of CO₂ into renewable hydrocarbon fuels: state-of-the-art accomplishment, challenges, and prospects, *Adv. Mater.* 26 (2014) 4607-4626.
- [4] Z. Bi, R. Guo, X. Hu, J. Wang, X. Chen, W. Pan, Research progress on photocatalytic reduction of CO₂ based on LDH materials, *Nanoscale* 14 (2022) 3367-3386.
- [5] S.N. Habisreutinger, L. Schmidt-Mende, J.K. Stolarczyk, Photocatalytic reduction of CO₂ on TiO₂ and other semiconductors, *Angew. Chem.* 52 (2013) 7372-7408.
- [6] N. Shehzad, M. Tahir, K. Johari, T. Murugesan, M. Hussain, A critical review on TiO₂ based photocatalytic CO₂ reduction system: strategies to improve efficiency, *J. CO₂ Util.* 26 (2018) 98-122.
- [7] H. Liu, H. Song, W. Zhou, X. Meng, J. Ye, A promising application of optical hexagonal TaN in photocatalytic reactions, *Angew. Chem.* 130 (2018) 17023-17026.
- [8] A. Akhundi, A. Habibi-Yangjeh, M. Abitorabi, S.R. Pourn, Review on photocatalytic conversion of carbon dioxide to value-added compounds and renewable fuels by graphitic carbon nitride-based photocatalysts, *Catal. Rev. Sci. Eng.* 61 (2019) 595-628.
- [9] T. Takata, C. Pan, K. Domen, Recent progress in oxynitride photocatalysts for visible-light-driven water splitting, *Sci. Technol. Adv. Mater.* 16 (2015) 033506.
- [10] J. Song, Y. Lu, Y. Lin, Q. Liu, X. Wang, W. Su, A direct Z-scheme α -Fe₂O₃/LaTiO₂N visible-light photocatalyst for enhanced CO₂ reduction activity, *Appl. Catal. B* 292 (2021) 120185.
- [11] A. Nakada, T. Nakashima, K. Sekizawa, K. Maeda, O. Ishitani, Visible-light-driven CO₂ reduction on a hybrid photocatalyst consisting of a Ru(II) binuclear complex and a Ag-loaded TaON in aqueous solutions, *Chem. Sci.* 7 (2016) 4364-4371.
- [12] K. Sekizawa, K. Maeda, K. Domen, K. Koike, O. Ishitani, Artificial Z-Scheme constructed with a supramolecular metal complex and semiconductor for the photocatalytic reduction of CO₂, *J. Am. Chem. Soc.* 135 (2013) 4596-4599.

- [13] L. Pei, Y. Yuan, W. Bai, T. Li, H. Zhu, Z. Ma, J. Zhong, S. Yan, Z. Zou, In situ-grown island-shaped hollow graphene on TaON with spatially separated active sites achieving enhanced visible-light CO₂ reduction, *ACS Catal.* 10 (2020) 15083-15091.
- [14] S. Akrami, P. Edalati, M. Fuji, K. Edalati, High-entropy ceramics: review of principles, production and applications, *Mater. Sci. Eng. R: Rep.* 146 (2021) 100644.
- [15] C. Oses, C. Toher, S. Curtarolo, High-entropy ceramics, *Nat. Rev. Mater.* 5 (2020) 295-309.
- [16] S.H. Albedwawi, A. AlJaberi, G.N. Haidemenopoulos, K. Polychronopoulou, High entropy oxides-exploring a paradigm of promising catalysts: a review, *Mater. Des.* 202 (2021) 109534.
- [17] D. Wang, Z. Liu, S. Du, Y. Zhang, H. Li, Z. Xiao, W. Chen, R. Chen, Y. Wang, Y. Zou, Low-temperature synthesis of small-sized high-entropy oxides for water oxidation, *J. Mater. Chem. A* 7 (2019) 24211-24216.
- [18] Z. Ding, J. Bian, S. Shuang, X. Liu, Y. Hu, C. Sun, Y. Yang, High entropy intermetallic-oxide core-shell nanostructure as superb oxygen evolution reaction catalyst, *Adv. Sustain. Syst.* 4 (2020) 1900105.
- [19] G. Fang, J. Gao, J. Lv, H. Jia, H. Li, W. Liu, G. Xie, Z. Chen, Y. Huang, Q. Yuan, X. Liu, X. Lin, S. Sun, H.J. Qiu, Multi-component nanoporous alloy/(oxy)hydroxide for bifunctional oxygen electrocatalysis and rechargeable Zn-air batteries, *Appl. Catal. B* 268 (2020) 118431.
- [20] F. Okejiri, Z. Zhang, J. Liu, M. Liu, S. Yang, S. Dai, Room-temperature synthesis of high-entropy perovskite oxide nanoparticle catalysts through ultrasonication-based method, *ChemSusChem* 13 (2020) 111-115.
- [21] H. Xu, Z. Zhang, J. Liu, C.L. Do-Thanh, H. Chen, S. Xu, Q. Lin, Y. Jiao, J. Wang, Y. Wang, Y. Chen, S. Dai, Entropy-stabilized single-atom Pd catalysts via high-entropy fluorite oxide supports, *Nat. Commun.* 11 (2020) 3908.
- [22] H. Chen, K. Jie, C.J. Jafta, Z. Yang, S. Yao, M. Liu, Z. Zhang, J. Liu, M. Chi, J. Fu, S. Dai, An ultrastable heterostructured oxide catalyst based on high-entropy materials: a new strategy toward catalyst stabilization via synergistic interfacial interaction, *Appl. Catal. B* 276 (2020) 119155.
- [23] Y. Zheng, Y. Yi, M. Fan, H. Liu, X. Li, R. Zhang, M. Li, Z.A. Qiao, A High-entropy metal oxide as chemical anchor of polysulfide for lithium-sulfur batteries, *Energy Storage Mater.* 23 (2019) 678-683.
- [24] H. Chen, W. Lin, Z. Zhang, K. Jie, D.R. Mullins, X. Sang, S.Z. Yang, C.J. Jafta, C.A. Bridges, X. Hu, Mechanochemical synthesis of high entropy oxide materials under ambient conditions: dispersion of catalysts via entropy maximization, *ACS Mater. Lett.* 1 (2019) 83-88.
- [25] M.S. Lal, R. Sundara, High entropy oxides - a cost-effective catalyst for the growth of high yield carbon nanotubes and their energy applications, *ACS Appl. Mater. Interfaces* 11 (2019) 30846-30857.
- [26] Y. Shu, J. Bao, S. Yang, X. Duan, P. Zhang, Entropy-stabilized metal-CeO_x solid solutions for catalytic combustion of volatile organic compounds, *AIChE J.* 67 (2021) e17046.
- [27] P. Edalati, Q. Wang, H. Razavi-Khosroshahi, M. Fuji, T. Ishihara, K. Edalati, Photocatalytic hydrogen evolution on a high-entropy oxide, *J. Mater. Chem. A* 8 (2020) 3814-3821.
- [28] S. Akrami, Y. Murakami, M. Watanabe, T. Ishihara, M. Arita, M. Fuji, K. Edalati, Defective high-entropy oxide photocatalyst with high activity for CO₂ conversion, *Appl. Catal. B* 303 (2022) 120896.
- [29] O.F. Dippo, N. Mesgarzadeh, T.J. Harrington, G.D. Schrader, K.S. Vecchio, Bulk high-entropy nitrides and carbonitrides, *Sci. Rep.* 10 (2020) 21288.

- [30] T. Jin, X. Sang, R.R. Unocic, R.T. Kinch, X. Liu, J. Hu, H. Liu, S. Dai, Mechanochemical-assisted synthesis of high-entropy metal nitride via a soft urea strategy, *Adv. Mater.* 30 (2018) 1707512.
- [31] C.Y. He, X.L. Qiu, D.M. Yu, S.S. Zhao, H.X. Guo, G. Liu, X.H. Gao, Greatly enhanced solar absorption via high entropy ceramic AlCrTaTiZrN based solar selective absorber coatings, *J. Materiomics* 7 (2021) 460-469.
- [32] D.D. Le, S.K. Hong, T.S. Ngo, J. Le, Y.C. Park, S.I. Hong, Y.S. Na, Microstructural investigation of CoCrFeMnNi high entropy alloy oxynitride films prepared by sputtering using an air gas, *Met. Mater. Int.* 24 (2018) 1285-1292.
- [33] P. Edalati, X.F. Shen, M. Watanabe, T. Ishihara, M. Arita, M. Fuji, K. Edalati, High-entropy oxynitride as low-bandgap and stable photocatalyst for hydrogen production, *J. Mater. Chem. A* 9 (2021) 15076-15086.
- [34] K. Edalati, Z. Horita, A review on high-pressure torsion (HPT) from 1935 to 1988, *J. Mater. Sci. Eng. A* 652 (2016) 325-352.
- [35] K. Edalati, A. Bachmaier, V.A. Beloshenko, Y. Beygelzimer, V.D. Blank, W.J. Botta, K. Bryła, J. Čížek, S. Divinski, N.A. Enikeev, Y. Estrin, G. Faraji, R.B. Figueiredo, M. Fuji, T. Furuta, T. Grosdidier, J. Gubicza, A. Hohenwarter, Z. Horita, J. Huot, Y. Ikoma, M. Janeček, M. Kawasaki, P. Král, S. Kuramoto, T.G. Langdon, D.R. Leiva, V.I. Levitas, A. Mazilkin, M. Mito, H. Miyamoto, T. Nishizaki, R. Pippan, V.V. Popov, E.N. Popova, G. Purcek, O. Renk, Á. Révész, X. Sauvage, V. Sklenicka, W. Skrotzki, B.B. Straumal, S. Suwas, L.S. Toth, N. Tsuji, R.Z. Valiev, G. Wilde, M.J. Zehetbauer, X. Zhu, Nanomaterials by severe plastic deformation: review of historical developments and recent advances, *Mater. Res. Lett.* 10 (2022) 163-256.
- [36] J. Low, J. Yu, M. Jaroniec, S. Wageh, A.A. Al-Ghamdi, Heterojunction photocatalysts, *Adv. Mater.* 29 (2017) 1601694.
- [37] Y. Wang, H. Huang, Z. Zhang, C. Wang, Y. Yang, Q. Li, D. Xu, Lead-free perovskite Cs₂AgBiBr₆@g-C₃N₄ Z-scheme system for improving CH₄ production in photocatalytic CO₂ reduction, *Appl. Catal. B* 282 (2021) 119570.
- [38] S. Akrami, M. Watanabe, T.H. Ling, T. Ishihara, M. Arita, M. Fuji, K. Edalati, High pressure TiO₂-II polymorph as an active photocatalyst for CO₂ to CO conversion, *Appl. Catal. B* 298 (2021) 120566.
- [39] X. Li, J. Yu, M. Jaroniec, Hierarchical photocatalysts, *Chem. Soc. Rev.* 45 (2016) 2603-2636.
- [40] L.Y. Lin, S. Kavadiya, X. He, W.N. Wang, B.B. Karakocak, Y.C. Lin, M.Y. Berezin, P. Biswas, Engineering stable Pt nanoparticles and oxygen vacancies on defective TiO₂ via introducing strong electronic metal-support interaction for efficient CO₂ photoreduction, *Chem. Eng. J.* 389 (2020) 123450.
- [41] L. Liu, H. Zhao, J. Andino, Y. Li, Photocatalytic CO₂ Reduction with H₂O on TiO₂ Nanocrystals: Comparison of Anatase, Rutile, and Brookite Polymorphs and Exploration of Surface Chemistry, *ACS Catal.* 2 (2012) 1817-1828.
- [42] K. Wang, J. Lu, Y. Lu, C.H. Lau, Y. Zheng, X. Fan, Unravelling the C-C coupling in CO₂ photocatalytic reduction with H₂O on Au/TiO_{2-x}: combination of plasmonic excitation and oxygen vacancy, *Appl. Catal. B* 292 (2021) 120147.
- [43] A.A. Davydov, *Infrared Spectroscopy of Adsorbed Species on the Surface of Transition Metal Oxides*, Wiley and Sons, Chichester, UK, 1990.
- [44] Y. Pan, P. Kuai, Y. Liu, Q. Geb, C. Liu, Promotion effects of Ga₂O₃ on CO₂ adsorption and conversion over a SiO₂-supported Ni catalyst, *Energy Environ. Sci.* 3 (2010) 1322-1325.

- [45] M.A.A. Aziz, A.A. Jalil, S. Wongsakulphasatch, D.V.N. Vo, Understanding the role of surface basic sites of catalysts in CO₂ activation in dry reforming of methane: a short review, *Catal. Sci. Technol.* 10 (2020) 35-45.
- [46] H. Lu, J. Tournet, K. Dastafkan, Y. Liu, Y.H. Ng, S.K Karuturi, C. Zhao, Z. Yin, Noble-metal-free multicomponent nanointegration for sustainable energy conversion, *Chem. Rev.* 121 (2021) 10271-10366.
- [47] Y. Sun, S. Dai, High-entropy materials for catalysis: A new frontier, *Sci. Adv.* 7 (2021) 20.
- [48] Z. Miao, G. Wang, X. Zhang, X. Dong, Oxygen vacancies modified TiO₂/Ti₃C₂ derived from MXenes for enhanced photocatalytic degradation of organic pollutants: the crucial role of oxygen vacancy to schottky junction, *Appl. Surf. Sci.* 528 (2020) 146929.
- [49] S. Akrami, Y. Murakami, M. Watanabe, T. Ishihara, M. Arita, Q. Guo, M. Fuji, K. Edalati, Enhanced CO₂ conversion on highly-strained and oxygen-deficient BiVO₄ photocatalyst, *Chem. Eng. J.* 442 (2022) 136209.
- [50] A. Crake, K.C. Christoforidis, R. Godin, B. Moss, A. Kafizas, S. Zafeirotos, J.R. Durrant, C. Petit, Titanium dioxide/carbon nitride nanosheet nanocomposites for gas phase CO₂ photoreduction under UV-visible irradiation, *Appl. Catal. B* 242 (2019) 369-378.
- [51] Y. Wang, Y. Chen, Y. Zuo, F. Wang, J. Yao, B. Li, S. Kang, X. Li, L. Cui, Hierarchically mesostructured TiO₂/graphitic carbon composite as a new efficient photocatalyst for the reduction of CO₂ under simulated solar irradiation, *Catal. Sci. Technol.* 3 (2013) 3286-3291.
- [52] Z. He, L. Wen, D. Wang, Y. Xue, Q. Lu, C. Wu, J. Chen, S. Song, Photocatalytic reduction of CO₂ in aqueous solution on surface-fluorinated anatase TiO₂ nanosheets with exposed {001} facets, *Energy Fuels* 28 (2014) 3982-3993.
- [53] Y. Li, C. Wang, M. Song, D. Li, X. Zhang, Y. Liu, TiO_{2-x}/CoO_x Photocatalyst sparkles in photothermocatalytic reduction of CO₂ with H₂O steam, *Appl. Catal. B* 243 (2019) 760-770.
- [54] J. Jiao, Y. Wei, Y. Zhao, Z. Zhao, A. Duan, J. Liu, Y. Pang, J. Li, G. Jiang, Y. Wang, AuPd/3DOM-TiO₂ catalysts for photocatalytic reduction of CO₂: high efficient separation of photogenerated charge carriers, *Appl. Catal. B* 209 (2017) 228-239.
- [55] Z. Xiong, H.B. Wang, N.Y. Xu, H.L. Li, B.Z. Fang, Y.C. Zhao, J.Y. Zhang, C.G. Zheng, Photocatalytic reduction of CO₂ on Pt²⁺-Pt⁰/TiO₂ nanoparticles under UV/Vis light irradiation: a combination of Pt²⁺ doping and Pt nanoparticles deposition, *Int. J. Hydrogen Energy* 40 (2015) 10049-10062.
- [56] B.Z. Fang, A. Bonakdarpour, K. Reilly, Y.L. Xing, F. Taghipour, D.P. Wilkinson, Large-scale synthesis of TiO₂ microspheres with hierarchical nanostructure for highly efficient photodriven reduction of CO₂ to CH₄, *ACS Appl. Mater. Interfaces* 6 (2014) 15488-15498.
- [57] K. Li, L. Lin, T. Peng, Y. Guo, R. Li, J. Zhang, Asymmetric zinc porphyrin-sensitized nanosized TiO₂ for efficient visible-light-driven CO₂ photoreduction to CO/CH₄, *J. Chem. Commun.* 51 (2015) 12443-12446.
- [58] B.Z. Fang, Y.L. Xing, A. Bonakdarpour, S.C. Zhang, D.P. Wilkinson, Hierarchical CuO-TiO₂ hollow microspheres for highly efficient photodriven reduction of CO₂ to CH₄, *ACS sustainable. Chem. Eng.* 3 (2015) 2381-2388.
- [59] Z.Y. Zhang, Z. Wang, S.W. Cao, C. Xue, Au/Pt nanoparticle-decorated TiO₂ nanofibers with plasmon-enhanced photocatalytic activities for solar-to-fuel conversion, *J. Phys. Chem. C* 117 (2013) 25939-25947.
- [60] P. Xia, M. Antonietti, B. Zhu, T. Heil, J. Yu, S. Cao, Designing defective crystalline carbon nitride to enable selective CO₂ photoreduction in the gas phase, *Adv. Funct. Mater.* 29 (2019) 1900093.

- [61] E.A. Kozlova, M.N. Lyulyukin, D.V. Markovskaya, D.S. Selishchev, S.V. Cherepanova, D.V. Kozlov, Synthesis of $\text{Cd}_{1-x}\text{Zn}_x\text{S}$ photocatalysts for gas-phase CO_2 reduction under visible light, *Photochem. Photobiol Sci.* 18 (2019) 871-877.
- [62] L. Ye, H. Wang, X. Jin, Y. Su, D. Wang, H. Xie, X. Liu, X. Liu, Synthesis of olive-green few-layered BiOI for efficient photoreduction of CO_2 into solar fuels under visible/near-infrared light, *Sol. Energy Mater. Sol. Cells* 144 (2016) 732-739
- [63] H. Jiang, K. Katsumata, J. Hong, A. Yamaguchi, K. Nakata, C. Terashima, N. Matsushita, M. Miyauchi, A. Fujishima, Photocatalytic reduction of CO_2 on Cu_2O -loaded Zn-Cr layered double hydroxides, *Appl. Catal. B* 224 (2018) 783-790.
- [64] T. Ye, W. Huang, L. Zeng, M. Li, J. Shi, CeO_{2-x} platelet from monometallic cerium layered double hydroxides and its photocatalytic reduction of CO_2 , *Appl. Catal. B* 210 (2017) 141-148.
- [65] E. Pastor, F. Pesci, A. Reynal, A. Handoko, M. Guo, X. An, A. Cowan, D. Klug, J. Durrant, J. Tang, Interfacial charge separation in $\text{Cu}_2\text{O}/\text{RuO}_x$ as a visible light driven CO_2 reduction catalyst, *Phys. Chem. Chem. Phys.* 210 (2017) 141-148.
- [66] S. Guo, J. Di, C. Chen, C. Zhu, M. Duan, C. Lian, M. Ji, W. Zhou, M. Xu, P. Song, R. Long, X. Cao, K. Gu, J. Xia, H. Liu, Y. Zhao, L. Song, Y. Xiong, S. Li, Z. Liu, Oxygen vacancy mediated bismuth stannate ultra-small nanoparticle towards photocatalytic CO_2 -to-CO conversion, *Appl. Catal. B* 276 (2020) 119156.
- [67] Z. Duan, X. Zhao, C. Wei, L. Chen, Ag-Bi/BiVO₄ chain-like hollow microstructures with enhanced photocatalytic activity for CO_2 conversion, *Appl. Catal. A* 594 (2020) 117459.
- [68] Y. Chen, F. Wang, Y. Cao, F. Zhang, Y. Zou, Z. Huang, L. Ye, Y. Zhou, Interfacial oxygen vacancy engineered two-dimensional g-C₃N₄/BiOCl heterostructures with boosted photocatalytic conversion of CO_2 , *ACS Appl. Energy Mater.* 3 (2020) 4610-4618.
- [69] X.Y. Dao, X.F. Xie, J.H. Guo, X.Y. Zhang, Y.S. Kang, W.Y. Sun, Boosting photocatalytic CO_2 reduction efficiency by heterostructures of $\text{NH}_2\text{-MIL-101 (Fe)}/\text{g-C}_3\text{N}_4$, *ACS Appl. Energy Mater.* 3 (2020) 3946-3954.
- [70] X. Zhang, G. Ren, C. Zhang, R. Li, Q. Zhao, C. Fan, Photocatalytic reduction of CO_2 to CO over 3D Bi₂MoO₆ microspheres: simple synthesis, high efficiency and selectivity, reaction mechanism, *Catal. Lett.* 150 (2020) 2510-2516.
- [71] X. Jin, C. Lv, X. Zhou, L. Ye, H. Xie, Y. Liu, H. Su, B. Zhang, G. Chen, Oxygen vacancies engineering Bi₂₄O₃₁C₁₁₀ photocatalyst for boosted CO_2 conversion, *ChemSusChem.* 12 (2019) 2740-2747.
- [72] Y. Xie, Y. Zhuo, S. Liu, Y. Lin, D. Zuo, X. Wu, C. Li, P.K. Wong, Ternary g-C₃N₄/ZnNCN@ZIF-8 hybrid photocatalysts with robust interfacial interactions and enhanced CO_2 reduction, *Solar RRL.* 4 (2020) 1900440.
- [73] C. Kim, K.M. Cho, A. Al-Saggaf, I. Gereige, H.T. Jung, Z-scheme photocatalytic CO_2 conversion on three-dimensional BiVO₄/carbon-coated Cu_2O nanowire arrays under visible light, *ACS Catal.* 8 (2018) 4170-4177.
- [74] J. Wang, C. Qin, H. Wang, M. Chu, A. Zada, X. Zhang, J. Li, F. Raziq, Y. Qu, L. Jing, Exceptional photocatalytic activities for CO_2 conversion on AlO bridged g-C₃N₄/ α -Fe₂O₃ z-scheme nanocomposites and mechanism insight with isotopes Z, *Appl. Catal. B* 224 (2018) 459-466.
- [75] L.J. Liu, D.T. Pitts, H.L. Zhao, C.Y. Zhao, Y. Li, Silver-incorporated bicrystalline (anatase/brookite) TiO₂ microspheres for CO_2 photoreduction with water in the presence of methanol, *Appl. Catal. A* 467 (2013) 474-482.

- [76] M. Tahir, N.S. Amin, Indium-doped TiO₂ nanoparticles for photocatalytic CO₂ reduction with H₂O vapors to CH₄, *Appl. Catal. B* 162 (2015) 98-109.
- [77] M. Tahir, N.S. Amin, Photocatalytic reduction of carbon dioxide with water vapors over montmorillonite modified TiO₂ nanocomposites, *Appl. Catal. B* 142-143 (2013) 512-522.
- [78] Y. Bai, P. Yang, L. Wang, B. Yang, H. Xie, Y. Zhou, L. Ye, Ultrathin Bi₄O₅Br₂ nanosheets for selective photocatalytic CO₂ conversion into CO, *Chem. Eng. J.* 360 (2019) 473-482.
- [79] D. Maiti, A.J. Meier, J. Cairns, S. Ramani, K. Martinet, J.N. Kuhn, V.R. Bhethanabotla, Intrinsically strained noble metal-free oxynitrides for solar photoreduction of CO₂, *Dalton Trans.* 48 (2019) 12738-12748.
- [80] N. Lin, Y. Lin, X. Qian, X. Wang, W. Su, Construction of a 2D/2D WO₃/LaTiO₂N direct Z-scheme photocatalyst for enhanced CO₂ reduction performance under visible light, *ACS Sustainable Chem. Eng.* 9 (2021) 13686-1369.